Materials Today Bio 15 (2022) 100264

Contents lists available at ScienceDirect

Materials Today Bio

journal homepage: www.journals.elsevier.com/materials-today-bio

Architecting polyelectrolyte hydrogels with Cu-assisted polydopamine nanoparticles for photothermal antibacterial therapy

ZhangPing Li [a,1], Shengye You [b,1], Ruiting Mao [b], Yajing Xiang [b], Erya Cai [b], Hui Deng [b,**], Jianliang Shen [c,d,e,***], Xiaoliang Qi [c,*]

[a] The Quzhou Affiliated Hospital of Wenzhou Medical University, Quzhou People's Hospital, Quzhou, Zhejiang, 324000, China
[b] School & Hospital of Stomatology, Wenzhou Medical University, Wenzhou, Zhejiang, 325027, China
[c] State Key Laboratory of Ophthalmology, Optometry and Vision Science, School of Ophthalmology and Optometry, School of Biomedical Engineering, Wenzhou Medical University, Wenzhou, Zhejiang, 325027, China
[d] Wenzhou Institute, University of Chinese Academy of Sciences, Wenzhou, Zhejiang, 325000, China
[e] Oujiang Laboratory (Zhejiang Lab for Regenerative Medicine, Vision and Brain Health), Wenzhou, Zhejiang, 325001, China

ARTICLE INFO

Keywords:
Polydopamine nanoparticles
Cu nanoparticles
Polyelectrolyte hydrogel
Photothermal antibacterial treatment
Wound healing

ABSTRACT

Polydopamine nanoparticles (PDA NPs) are an appealing biomimetic photothermal agent for photothermal antibacterial treatment because of their long-term safety, excellent photostability, accessible manufacturing, and good biodegradability. However, the low photothermal conversion efficiency (PCE) of PDA NPs requires high-power and long-term near-infrared light irradiation, which severely restricts their practical application. In this work, PDA@Cu NPs were fabricated by growing Cu NPs in situ on the surface of PDA and then introduced into a polyelectrolyte hydrogel precursor (cationic polyethyleneimine/anionic pectin, named as CPAP). The formulated photothermal platform possessed a high PCE (55.4%), almost twice as much as pure PDA NPs (30.8%). Moreover, the designed CPAP/PDA@Cu captured and killed some bacteria by electrostatic adsorption, which helped enhance the antibacterial performance. As expected, the formed CPAP/PDA@Cu that combined the advantageous features of PDA@Cu NPs (high PCE) and CPAP matrix (inherent antibacterial activity and preventing NPs aggregation) can efficiently kill bacteria both *in vitro* and *in vivo* under the help of near-infrared laser irradiation. Taken together, this study offers a promising strategy for constructing a facile and safe PDA-based photothermal agent for photothermal antibacterial therapy.

1. Introduction

Pathogenic bacteria-related infections are one of the most severe risks in the fields of food and medicine, leading to nearly one-third of deaths worldwide and posing a severe threat to public health and economics [1,2]. As a most accepted treatment, antibiotics have been extensively utilized for bacterial infections. However, the indiscriminate utilization of antibiotics has been causing the emergence of many drug-resistant bacteria [3]. Therefore, developing effective alternative strategies to manage bacterial infections without inducing multi-drug resistance is urgently needed [4]. In recent years, various approaches such as photodynamic therapy, chemodynamic therapy, and photothermal therapy (PTT) have emerged to fight bacteria. Among these antibacterial approaches, PTT, which can efficiently kill bacteria by physical heating, has drawn substantial interest because of its outstanding high selectivity, non-invasive nature, preferable controllability, negligible drug resistance, and less likely to induce systemic toxicity [5,6]. Particularly, near-infrared (NIR) light-triggered PTT has been extensively developed owing to the excellent tissue penetration of NIR light [7,8]. In the PTT process, the NIR light energy can convert into heat with the help of photothermal agents (PTAs), providing a spatiotemporal thermal effect to cause bacterial degeneration in the light-irradiated area [9,10].

* Corresponding author. School of Ophthalmology and Optometry, School of Biomedical Engineering, Wenzhou Medical University, Wenzhou, Zhejiang, 325027, China.
** Corresponding author.
*** Corresponding author. School of Ophthalmology and Optometry, School of Biomedical Engineering, Wenzhou Medical University, Wenzhou, Zhejiang, 325027, China.
E-mail addresses: dh0726@163.com (H. Deng), shenjl@wiucas.ac.cn (J. Shen), xiaoliangqi90@gmail.com (X. Qi).
[1] These authors contributed equally to this work.

https://doi.org/10.1016/j.mtbio.2022.100264
Received 18 March 2022; Received in revised form 6 April 2022; Accepted 14 April 2022
Available online 20 April 2022

There are numerous organic NPs (PDA, polypyrrole, porphyrins, and cyanines) and inorganic materials (palladium nanosheets, carbon nanomaterials, transitional metal dichalcogenide, and gold NPs) that have been explored as PTAs for PTT [11–14]. Among these popular PTAs, PDA, a melanin-based biopolymer widely distributed in almost all kinds of living organisms, is the most potential one due to its superior biocompatibility, prominent biodegradability, favorable photostability, and ease of synthesis [15–18]. Recently, PDA nano-PTAs possessing various sizes (mainly from 20 to 500 nm) and different morphologies (nanosheets and nanospheres) have emerged for utilization in PTT [19–21]. Nevertheless, two inherent defects of PDA nano-PTAs severely hamper their clinical application. One is that PDA nano-PTAs are readily aggregated, which is mainly ascribed to the existence of many active groups (catechol, secondary amine, and primary amine moieties) on the surface of PDA. The light absorption efficiency of PDA decreases when it is aggregated. The other is that the PCE of PDA NPs at 808 nm is relatively low (nearly 20%) [22] and even lower at longer wavelengths due to the nonradiative conversion and insufficient light absorption of PDA in the NIR region [23]. Therefore, reducing the aggregation and improving the light absorption efficiency of PDA nanomaterials simultaneously are the main obstacles in realizing PDA PTAs with high photothermal conversion ability for bacterial infection treatment.

To achieve a PDA with robust photothermal performance, many efforts have been made in two aspects, including promoting the dispersion by incorporating PDA into a matrix and increasing the light absorption ability of PDA in the NIR region through improving non-radiative energy transfer [24]. For instance, Qi and co-workers demonstrated that PDA with high PTT efficacy was realized when PDA was introduced into an agarose hydrogel scaffold [25]. Furthermore, Cheng and co-workers found that PDA displayed augmented light absorption efficiency when the surface of PDA was decorated with metal NPs by in situ deposition [26]. The reason was that the addition of metal was beneficial to increasing the charge transfer efficiency of the PDA-based system. Inspired by these results, we speculate that integrating the surface modification with a suitable carrier may enhance the photothermal performance of PDA.

In light of the above considerations, in this study, we engineered a polyelectrolyte complex hydrogel composed of cationic polyethyleneimine (a water-soluble artificial polymer), anionic pectin (a class of plant polysaccharides widely used in food and medicine), and PDA@Cu NPs for antibacterial therapy. As shown in Scheme 1, PDA@Cu NPs were fabricated by the reduction-deposition of Cu ions on the surface of PDA NPs. With the assistance of Cu NPs, the PCE was almost doubled from 30.8% (PDA) to 54.2% (PDA@Cu). Subsequently, PDA@Cu NPs were introduced into the polyelectrolyte hydrogel precursor (cationic polyethyleneimine/anionic pectin, labeled as CPAP) to fabricate the CPAP/PDA@Cu hydrogel by a convenient one-step mixing approach. With the help of CPAP, PDA@Cu NPs were uniformly dispersed without agglomeration; besides, the CPAP matrix possessed abundant functional groups that can non-selectively capture and kill bacteria by hydrophobic, van der Waals forces, and electrostatic interactions, thus offering additional antibacterial activity. *In vitro* antibacterial assay exhibited that CPAP/PDA@Cu had broad-spectrum antibacterial activity against *Staphylococcus aureus* (98.2%) and *Escherichia coli* (100%). Furthermore, *in vivo* antibacterial assays also confirmed the prominent bactericidal ability of CPAP/PDA@Cu hydrogel. To the best of our knowledge, this is the first report on developing a CPAP/PDA@Cu system for photothermal therapy of bacterial infection. We believe that this study will provide new ideas for designing and applying robust PDA nano-photothermal agents for more bioapplications.

2. Materials and methods

2.1. Materials

High acyl anionic pectin (AP) was purchased from Henan Zhongtai (Zhengzhou, China). Cationic polyethyleneimine (CP, M_W = 70,000, 50 wt% in water), anhydrous ethanol, sodium hydroxide (NaOH), and ammonia solution (28 wt% in water) were obtained from Macklin (Shanghai, China). Copper chloride and dopamine hydrochloride were purchased from Aladdin (Shanghai, China). Agar powder, Luria-Bertani broth, ascorbic acid, and tryptone soya broth were purchased from Solarbio (Beijing, China). Fetal bovine serum (FBS), penicillin/streptomycin (P/S), trypsin-EDTA (0.25%), Dulbecco's modified Eagle's medium (DMEM), and phosphate-buffered saline (PBS, pH = 7.4) were bought from Gibco (Grand Island, USA). L7012 Live/Dead *Bac*Light Bacterial Viability Kit comprising SYTO9 and propidium iodide (PI) was purchased from Thermo Fisher Scientific (Waltham, USA). Cell Counting Kit-8 (CCK-8) was commercially available from Glpbio (Montclair, USA). Live/Dead Cell Viability Kit composed of Calcein-AM and PI was purchased from Yeasen (Shanghai, China). All chemical reagents were used as supplied without further purification.

2.2. Synthesis of PDA NPs

In this study, PDA NPs were fabricated according to previous reports [27,28]. In detail, the ammonia solution (1 mL) was mixed with anhydrous ethanol (20 mL) and deionized water (45 mL). Subsequently, dopamine hydrochloride (250 mg) in deionized water (5 mL) was incorporated into the aforementioned blended solution, and the reaction was allowed to continue at 37 °C for 24 h under gentle stirring. Next, PDA NPs were isolated by high-speed centrifugation (12,000 rpm, 8 min) and washed four times with deionized water. Lastly, the synthesized PDA NPs were diluted to 5 mg/mL for further use.

2.3. Synthesis of PDA@Cu NPs

PDA@Cu NPs were fabricated employing a facile reduction-deposition approach. Specifically, 0.25 g copper chloride dihydrate was incorporated into a 250 mL round-bottom flask equipped with 20 mL of deionized water. Then, the solution of copper chloride was heated to 85 °C, and its pH was adjusted to 7.0 using NaOH, followed by simultaneously dropping ascorbic acid solution (0.625 M) and PDA NPs suspension (10 mg/mL) under constant stirring (300 rpm). After 60 min of reaction, PDA@Cu NPs were acquired after centrifugation at 12,000 rpm for 8 min. The obtained PDA@Cu NPs were washed four times with deionized water, diluted to 5 mg/mL, and stored in a 4 °C refrigerator for further usage.

2.4. Synthesis of hydrogels

Hydrogels were formed through a simple one-step blended method. Typically, 4 mL of CP polysaccharide solution (2 mg/mL) was first mixed with 4 mL of AP polysaccharide solution (2 mg/mL), followed by introducing PDA@Cu NPs suspension (5 mg/mL). After being vigorously mixed for 3 min at room temperature, the mixture was kept overnight to allow gelation. Herein, hydrogels with (CP + AP): PDA@Cu volume ratios of 8:0, 8:1, 8:2, and 8:3 were designed (designated as CPAP, CPAP1, CPAP2, and CPAP3, respectively).

2.5. Structure characterization

The zeta potentials of prepared NPs were monitored by a particle size analyzer (ZEN3600, Malvern, UK). The morphology of specimens was characterized by the JEM-1230 transmission electron microscope (TEM, Jeol, Japan) and the SU-8010 scanning electron microscope (SEM, Hitachi, Japan); before lyophilization, all hydrogels were first immersed in deionized water until the hydrogel weight no longer changed. The chemical groups of specimens were analyzed employing a Fourier transform infrared (FTIR) spectrometer (Tensor II, Bruker, Germany). Ultraviolet–visible–near-infrared (UV–vis–NIR) spectra were performed on a spectrophotometer (Cary5000, Agilent, USA). Thermogravimetric

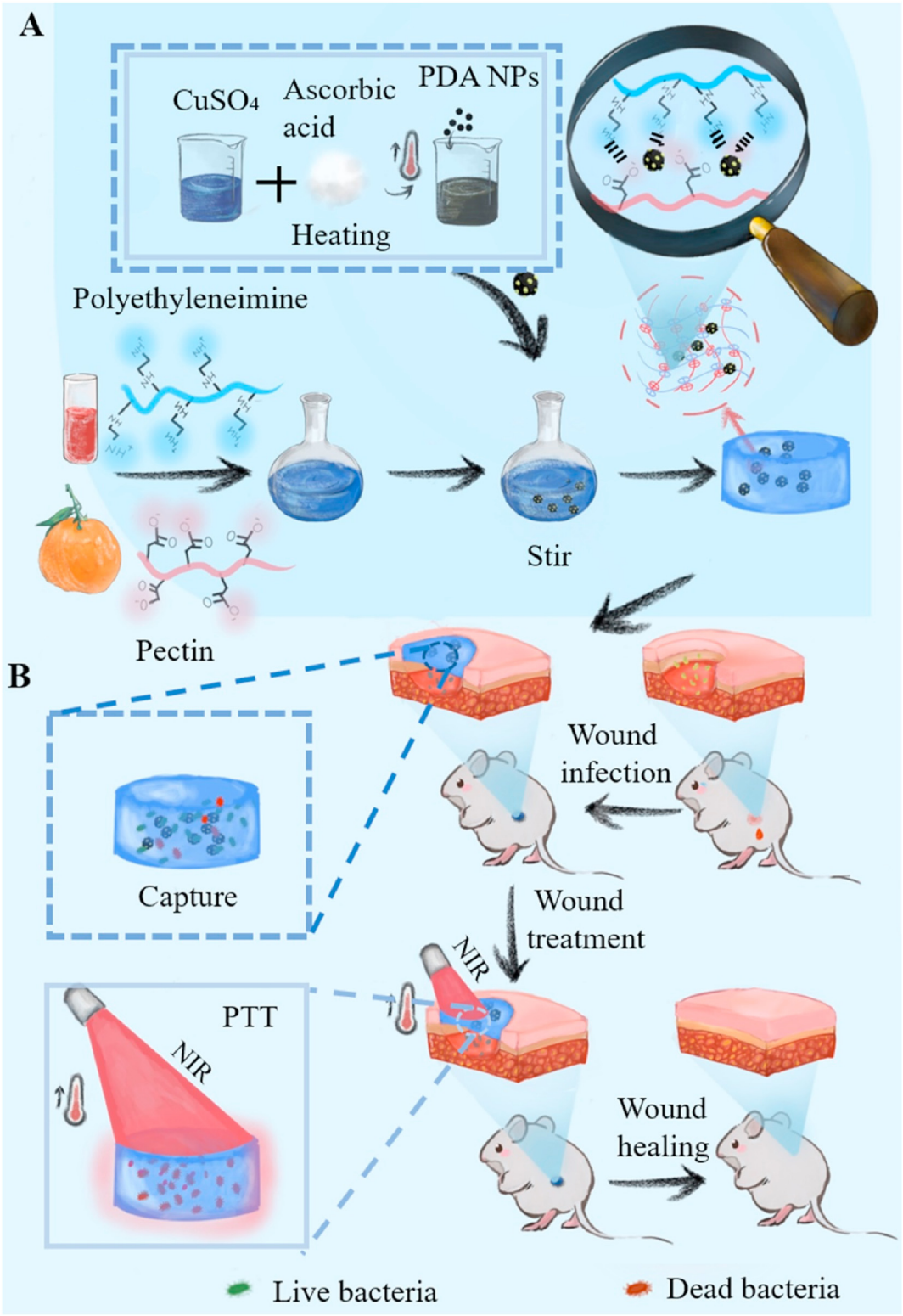

Scheme 1. Schematic illustrating the preparation (A) and antibacterial application (B) of CPAP/PDA@Cu hydrogel.

analysis (TGA) was conducted on a TGA8000 thermal gravimetric analyzer (PerkinElmer, USA) operating under a nitrogen atmosphere from 30 °C to 600 °C with a heating rate of 20 °C/min. The rheological properties of hydrogels were assessed using a DHR-2 rheometer (TA, USA). The rheological experiment was first conducted using a dynamic strain sweep test to detect the linear viscoelastic regions of prepared hydrogel samples (thickness = 2 mm, diameter = 25 mm). Then, the storage modulus (G′) and loss modulus (G″) of the designed specimens during alternate step-strain cycles between 1% and 1000% oscillation strain were assessed. Finally, dynamic frequency sweep tests of hydrogels were determined over a range of different angular frequencies (0.1–10 rad/s) with a fixed strain of 1%.

2.6. Swelling and water retention tests

The designed hydrogels were freeze-dried and weighed accurately (W_d) before measurements to explore the swelling properties. Then, these dried hydrogels were put into PBS at 37 °C until the equilibrium state was realized. Next, the hydrogels were taken out of the PBS and weighed (W_t) at certain intervals after removing the PBS on the hydrogel surface. Finally, the water uptake was calculated employing the following formula [29]:

$$\text{Water uptake} = (W_t - W_d)/W_d \quad (1)$$

Where W_t is the mass of the swollen hydrogel specimen and W_d is the mass of the initial hydrogel specimen.

Meanwhile, the water retention properties of designed CPAP/PDA@Cu hydrogel specimens were measured. Firstly, the hydrogel samples were soaked in PBS to reach the equilibrium of water uptake (M_0). Next, the hydrogels were transferred to an oven at 37 °C, and their weights (M_t) were weighed at a given time point. Finally, the water retention was calculated according to the following equation:

$$\text{Water retention } (\%) = M_t/M_0 \times 100\% \quad (2)$$

Where M_t is the mass of the gel sample at the specified duration and M_0 is the mass of the initial mass of the gel.

2.7. Photothermal performance measurement

An 808 nm NIR laser was adopted to evaluate the photothermal characteristics of the fabricated NPs and CPAP/PDA@Cu hydrogels. Typically, all specimens were put into 2.0 mL Eppendorf tubes and irradiated for 6 min using an 808 nm NIR at gradient power density (0.5, 1.0, and 2.0 W/cm^2). During the irradiation process, the temperature variation of the sample was monitored by an IR camera (E8, FLIR, USA). In addition, the stability of the specimens during the four repeated laser on-off cycles was also evaluated. As a result, the photothermal conversion efficiency was calculated as follows [30,31]:

$$\eta = \frac{hA\left(T_{max,spe} - T_{max,water}\right)}{I\left(1 - 10^{-A_{808}}\right)} \quad (3)$$

$$t = \frac{\sum_i m_i C_{P,i}}{hA} In\theta \quad (4)$$

$$\theta = \frac{T - T_{sur}}{T_{max} - T_{sur}} \quad (5)$$

where $T_{max,spe}$ denotes the maximum temperature of tested specimens; $T_{max,\ water}$ denotes the maximum temperatures of water; I denotes the laser power; A_{808} is the absorbance value of tested specimen aqueous solution at 808 nm; m_i denotes the water mass; $C_{p,i}$ denotes the water heat capacity; θ is the system constant.

2.8. In vitro antibacterial test

In this study, *Staphylococcus aureus* (*S. aureus*, ATCC 29213) and *Escherichia coli* (*E. coli*, ATCC 25922) were selected as the targeted bacteria to explore the antibacterial activity of CPAP/PDA@Cu hydrogel. Generally, the CPAP/PDA@Cu circular hydrogel with a diameter of 8 mm was first pre-soaked in PBS until achieving absorptive equilibrium. Then, it was sterilized with a UV lamp for 20 min and added into a 5.0 mL centrifuge tube containing bacterial suspension (1 mL, 1.0 × 10^7 CFU/mL). After co-culturing at 37 °C for 2 h, the tube was treated with or without irradiation (808 nm NIR, 1.0 W/cm^2) for 5 min. Simultaneously, the bacteria suspension treated by PBS with or without 808 nm NIR irradiation was acted as control groups. Next, 100 μL of bacteria solution was taken out from the tube and diluted. Subsequently, 100 μL of the diluted bacterial suspension was coated evenly on the agar plates and cultivated for 12 h. Ultimately, the agar plates were photographed by a digital camera, and the bacterial number was measured using a colony counter (J3, Tenlin, China).

Besides, we performed the bacterial live/dead staining assay to study the antibacterial properties of hydrogels. Briefly, after different treatments, the bacteria cells were co-stained by fluorescence dyes composed of SYTO9 and PI for 20 min in the dark. After being washed with PBS 3 times, the cell membrane integrity of the bacteria was observed employing a confocal laser scanning microscopy (CLSM, A1 imaging system, Nikon, Japan). All STYO9-stained bacteria displayed green fluorescence following the manufacturer's instructions, while PI-labeled dead bacteria emitted red fluorescence [32].

Additionally, the bacteria morphological changes after different treatments were captured by SEM for further investigating the sterilization routes of prepared hydrogels. Typically, the treated bacteria were collected, washed with PBS four times, fixed with glutaraldehyde, serially dehydrated with graded ethanol solutions (20–100%), sputter-coated with platinum to increase conductivity, and observed with SEM.

2.9. In vitro cytotoxicity test

The cytotoxicity of CPAP/PDA@Cu hydrogels on L929 cells was determined by employing a CCK-8 assay. First, the fabricated hydrogels were sterilized with UV light, then added into a DMEM containing 1% P/S and 10% FBS for 24 h to obtain the hydrogel extract liquid. Then, 100 μL of L929 cells (1 × 10^5 cells/mL) was aspirated into 96-well plates and incubated in an incubator (5% CO_2, 37 °C) overnight. Subsequently, the cell culture medium in each well was discarded, and the hydrogel leaching liquid was added and incubated for 1, 3, and 5 days. Next, the old cell culture medium was substituted by an equivalent fresh medium containing 10% CCK-8. After being incubated for 4 h, the optical density (OD) value of each well was detected at a wavelength of 450 nm. The L929 cells cultured without hydrogel extract liquid were defined as the control group. The cytotoxicity was determined from the formula below:

$$\text{Cell viability } (\%) = As/_{Ac} \times 100\% \quad (6)$$

Where A_s and A_c mean the absorbance values of the experimental specimen and the control specimen at 450 nm, respectively.

Additionally, we conducted a cell live/dead staining assay to qualitatively investigate the cell viability of the CPAP/PDA@Cu hydrogels. Briefly, after different treatments, the L929 cells were stained with calcein-AM/PI for 20 min. Subsequently, the fluorescent photos were collected employing CLSM. The dead cells with compromised plasma membranes showed red fluorescence, while viable cells with esterase activity displayed green fluorescence [33,34].

2.10. In vitro blood compatibility

The hemolysis rate of CPAP/PDA@Cu hydrogels was determined using red blood cells isolated from the eyeballs of healthy rats. First, diluted red blood cells (1 mL) were mixed using deionized water (100 mg) as the positive control, PBS (100 mg) as the negative control, and hydrogels (100 mg) as the experimental groups. Then, after incubating at 37 °C for 3 h, the supernatant absorbance at the wavelength of 545 nm was monitored on a UV–vis–NIR spectrometer. The tests were repeated three times. The hemolysis rate was calculated by the following formula [35]:

$$\textit{Hemolysis ratio } (\%) = \frac{(A_e - A_n)}{(A_p - A_n)} \times 100\% \quad (7)$$

where A_e, A_n, and A_p are the supernatant fraction absorbance of the experimental group (hydrogel), negative group (PBS), and positive group (deionized water), respectively.

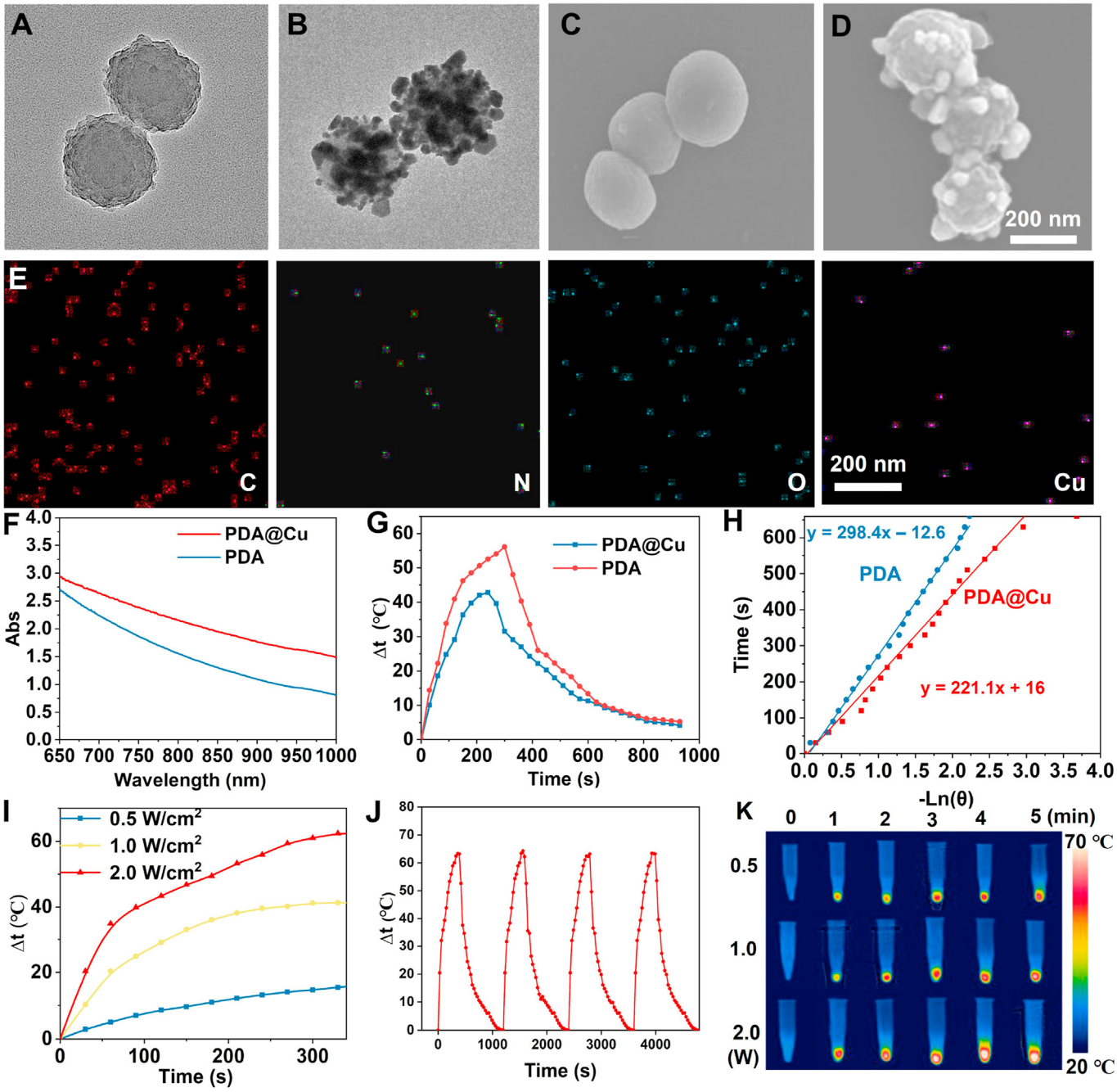

Fig. 1. Characterization of PDA@Cu NPs. TEM pictures of PDA NPs (A) and PDA@Cu NPs (B). SEM pictures of PDA NPs (C) and PDA@Cu NPs (D). (E) SEM elemental mapping photographs of PDA@Cu NPs. (F) UV–vis–NIR absorption spectra of PDA and PDA@Cu NPs. (G) Plot fitting of driving force temperature and cooling time. (H) The relationship between the time and –Lnθ. (I) The photothermal temperature rise of the PDA@Cu NPs under various powers of NIR irradiation (2.0, 1.0, and 0.5 W/cm^2). (J) Photothermal stability capability of PDA@Cu under repeated laser on-off of 2.0 W/cm^2 808 nm NIR irradiation. (K) Infrared thermal images of tested samples under different power NIR irradiation (2.0, 1.0, and 0.5 W/cm^2).

2.11. *In vivo photothermal performance*

All laboratory animal procedures had been reviewed and approved by the Institutional Animal Care and Use Committee of Wenzhou Medical University. Male Sprague-Dawley rats were kindly provided by Vital River Laboratory Animal Technology Co, Ltd (Beijing, China). Rats were randomly divided into three groups: PBS, CPAP hydrogel and CPAP3 hydrogel. Full-thickness circular wounds (diameter = 8 mm) were constructed on the shaved backs of each rat and were applied with PBS, CPAP hydrogel, and CPAP3 hydrogel. The wounds were then exposed to a NIR laser (808 nm, 1.0 W/cm^2) for 3 min. At last, the wound sites were photographed employing a thermal infrared camera.

2.12. *In vivo hemostatic experiment*

To assess the hemostatic potential of the hydrogels, rats were randomly divided into three groups: gauze, PBS, and CPAP3. Firstly, a bleeding model was made by cutting off the rat tail. Immediately after surgery, the bleeding site was covered with tested samples. Blood was carefully collected using a pre-weighed dry filter paper. Next, the wound

without hydrogel and gauze treatment was applied as the control group. After treating for 3 min, the total amount of lost blood was calculated by weighing the filter paper.

2.13. In vivo wound healing experiment

A bacteria-infected rat wound model was adopted to investigate the ability of the CPAP/PDA@Cu hydrogels to repair wounds. Firstly, round wounds with a diameter of 8 mm were produced on the back of the rats. Then, *S. aureus* suspension (10 μL, 1.0×10^8 CFU/mL) was inoculated into the created wounds and homogeneously smeared over the wound surface. Next, the bacterially infected wounds were covered with 100 μL of samples and classified into four test groups: negative control group (PBS), positive control group (3M Tegaderm hydrogel), CPAP3 hydrogel (100 μL), and CPAP3 hydrogel + NIR (1.0 W/cm^2, 3 min). Finally, hydrogels on the wounds were immobilized using medical tape. Photographs of the wounds were recorded every 24 h for 12 days. Meanwhile, bacteria at the wound sites were collected, and their numbers were determined using a plate counting approach. Besides, the regenerated skin tissues were excised and collected on days 3, 7, and 12 for Masson's trichrome, hematoxylin and eosin (H&E), and immunohistochemical (IL-6 and CD31) analyses [36].

2.14. Statistical analysis

All experiments in this work were conducted at least in three independent batches. All data were processed by OriginPro 8.0 and presented as the mean value ± standard deviation (SD). The data were considered statistically significant when $^*P < 0.05$ [37], and the data were recognized highly significant when $^{**}P < 0.01$ and $^{***}P < 0.001$.

3. Results and discussions

3.1. Synthesis and characterization of PDA@Cu NPs

In this study, PDA@Cu NPs were fabricated by a facile redox reaction method. Herein, Cu NPs were selected because they had good photoelectric properties, and we expected that the deposition of Cu NPs onto

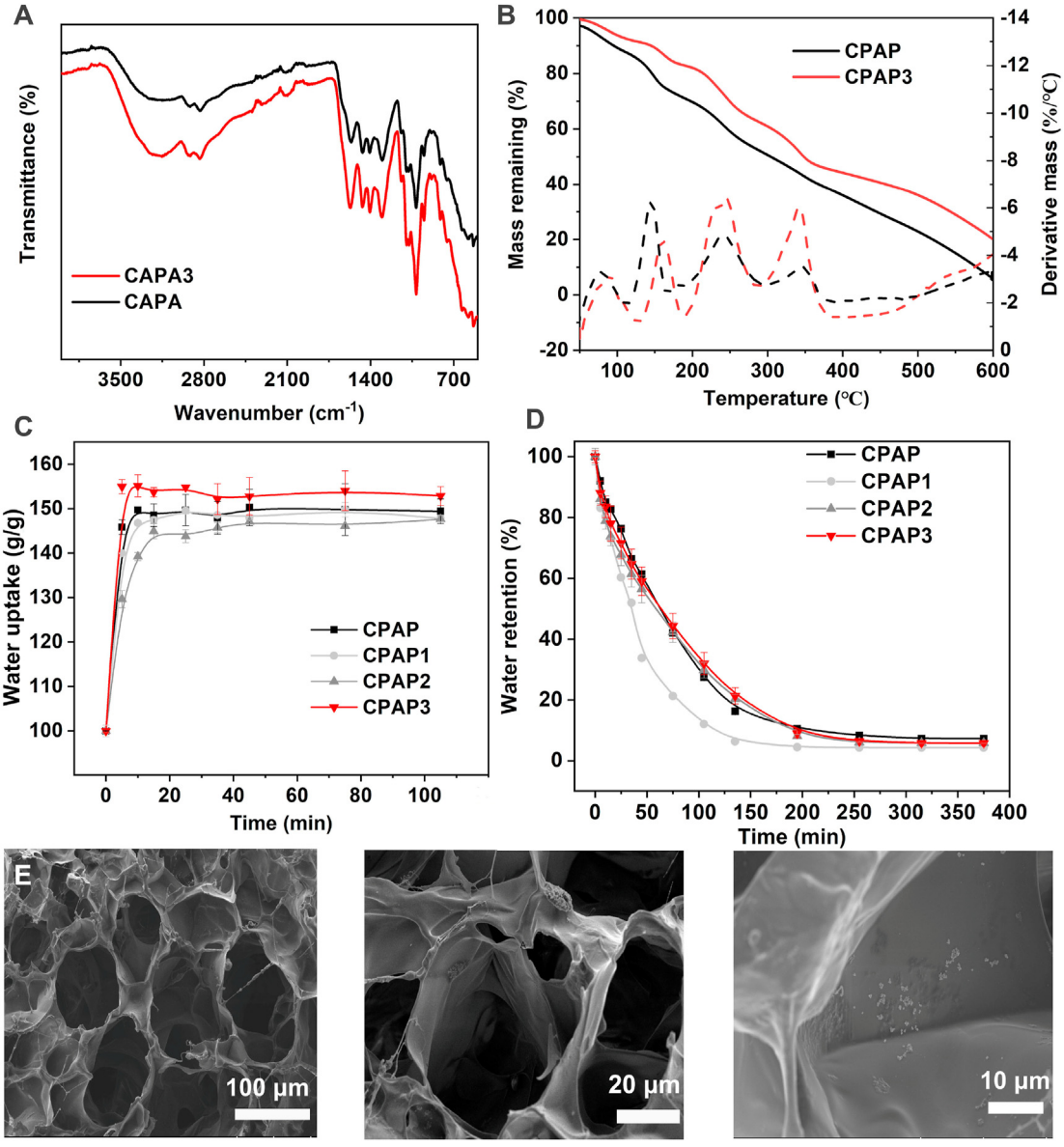

Fig. 2. Characterization of fabricated CPAP/PDA@Cu hydrogels. FTIR (A), TGA results (B), water retention (C), and water uptake (D) of CPAP/PDA@Cu hydrogels. (E) SEM image and its higher magnification image of CPAP/PDA@Cu hydrogel.

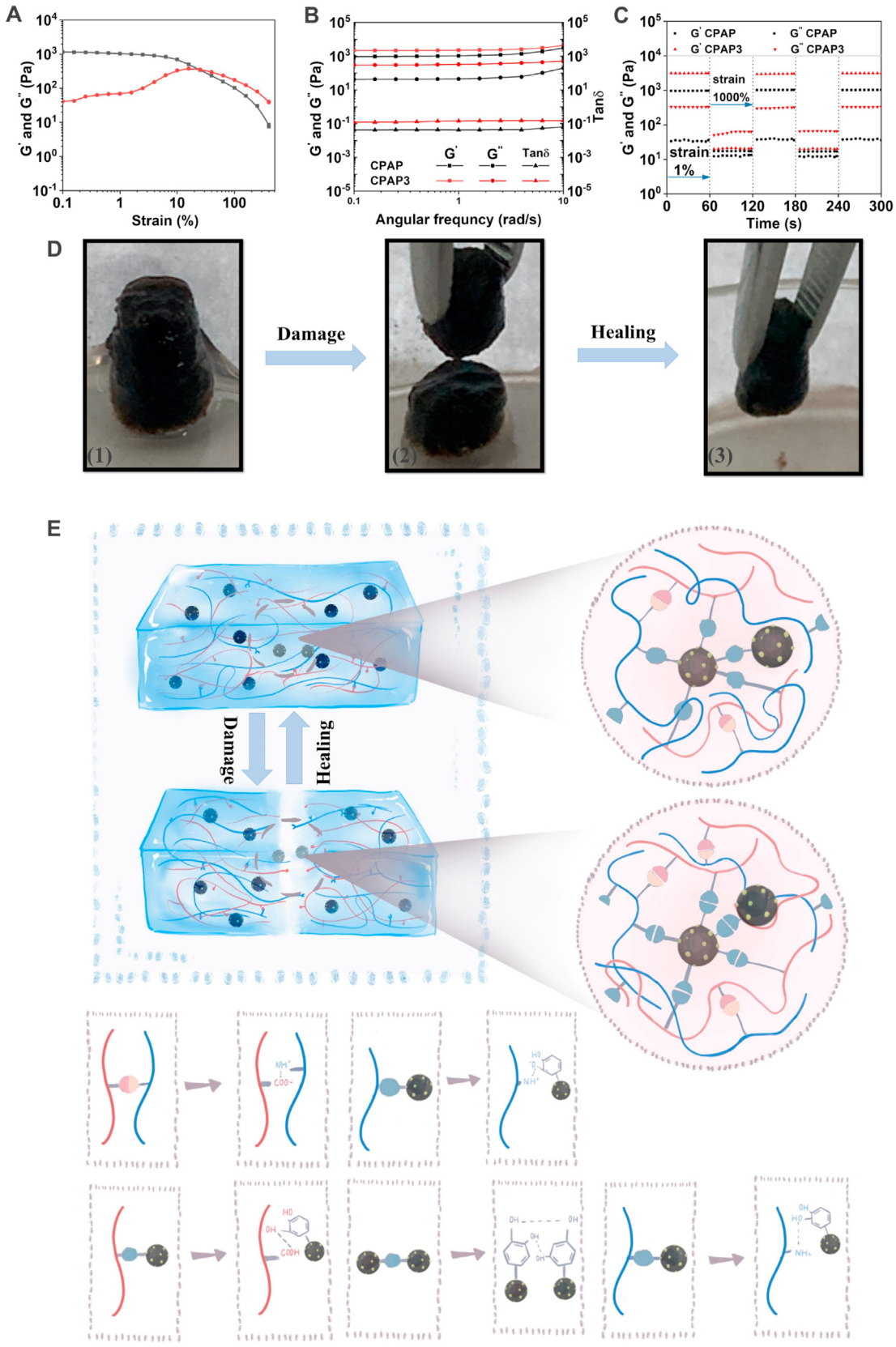

Fig. 3. Rheological performance and self-healing mechanism of designed CPAP/PDA@Cu hydrogels. Frequency sweep (A), viscosity (B), and dynamic step–strain (C) measurements of designed hydrogels. (D) Images of the self-healing process of CPAP/PDA@Cu. (E) Possible self-healing mechanism of CPAP/PDA@Cu.

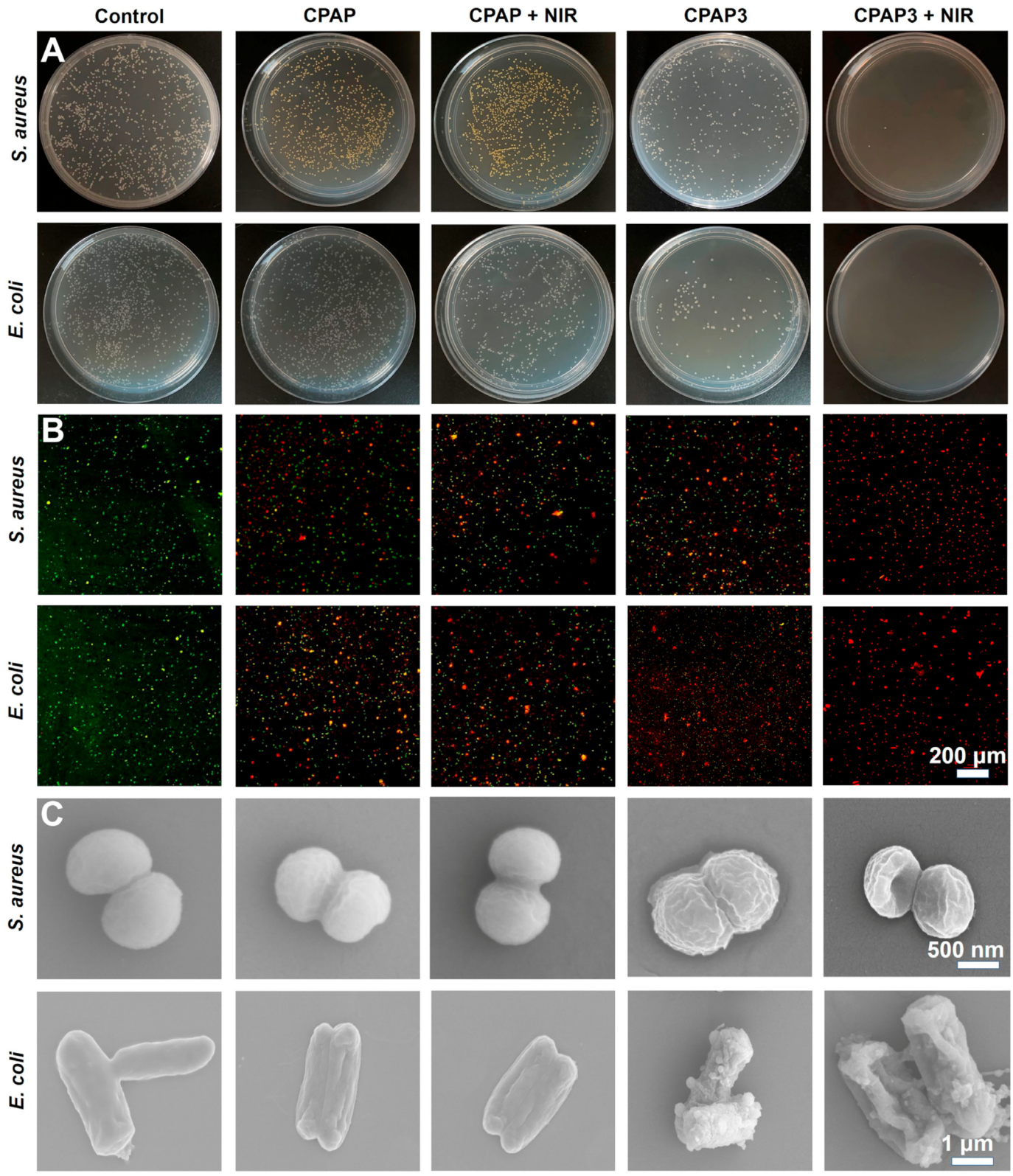

Fig. 4. *In vitro* antibacterial activity of different specimens. The colonization (A), confocal fluorescence (B), and SEM (C) images of *S. aureus* and *E. coli* after treatments with PBS, CPAP, CPAP + NIR, CPAP3, and CPAP3 + NIR.

the PDA surface might improve the photothermal conversion performance of PDA NPs. As displayed in Scheme 1, the deposition of Cu NPs was easily achieved because PDA possessed a variety of functional groups like dihydroxyphenyl groups, which can attract Cu^{2+} ions and actively participate in the reduction process of Cu^{2+}, forming coordination bonds with Cu NPs.

Firstly, the zeta potential of PDA NPs and PDA@Cu NPs was identified and evaluated. As presented in Fig. S1, the zeta potential of PDA NPs and

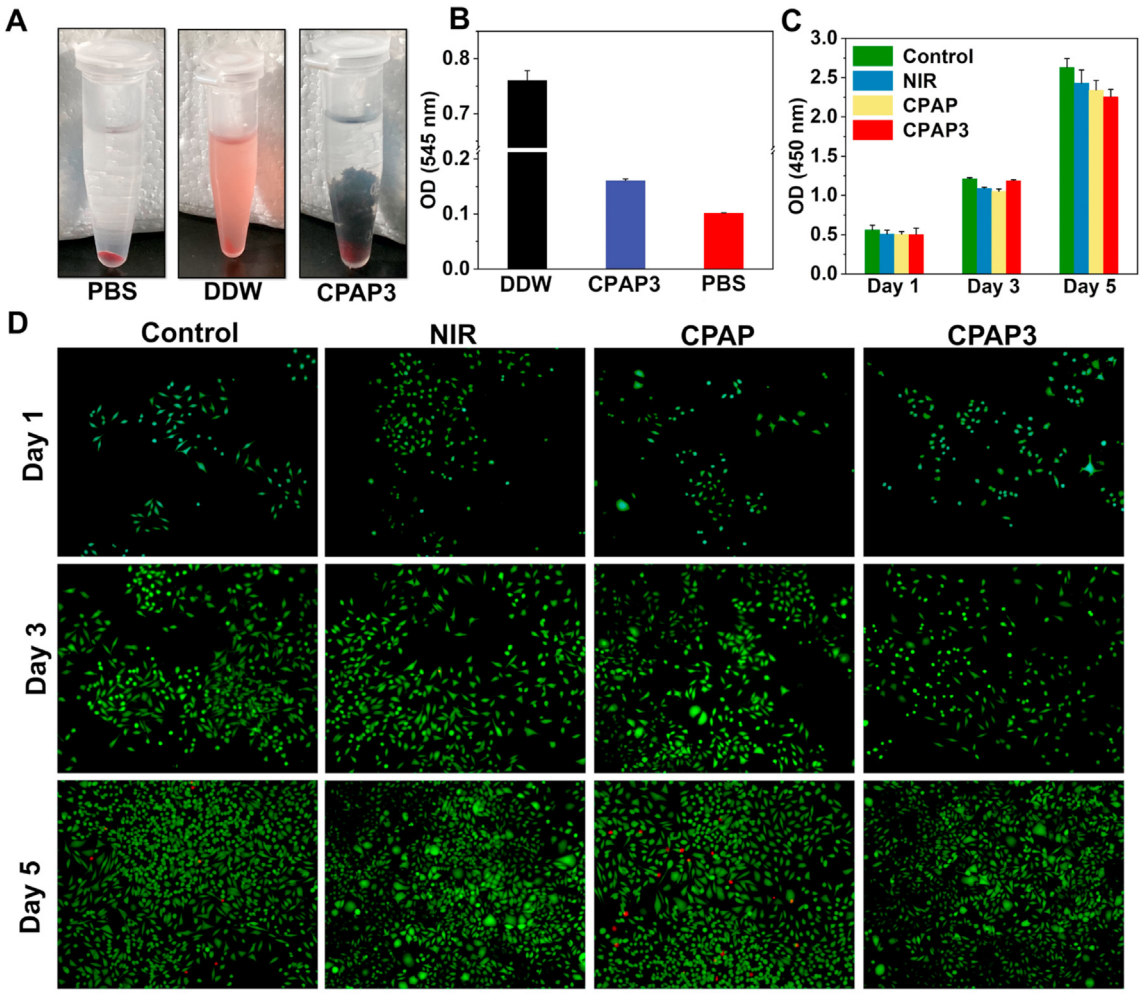

Fig. 5. *In vitro* biocompatibility assay. (A) Photographs from hemolysis test on PBS, DDW, and CPAP/PDA@Cu. (B) *In vitro* hemolysis of rat red blood cells in the presence of different specimens (n = 3). (C) *In vitro* cytotoxicity to L929 cells was measured by CCK-8 after exposure to different specimens for 1 day, 3 days, and 5 days (n = 3). (D) CLSM pictures of L929 cells double-stained with calcium-AM and PI after treating with different specimens for 1 day, 3 days, and 5 days. (For interpretation of the references to colour in this figure legend, the reader is referred to the Web version of this article.)

PDA@Cu NPs was −50.1 mV and −10.5 mV, respectively. This was because when Cu^{2+} was reduced to Cu, a certain number of negatively charged moieties of PDA were consumed. Thus, the zeta potential of PDA@Cu increased. After that, the morphology of the prepared PDA and PDA@Cu NPs was observed by TEM and SEM (Fig. 1A–D). Cu NPs (average diameter around 30 nm) were uniformly dispersed on the PDA surface, and Cu-modified PDA NPs exhibited a relatively homogeneously spherical architecture with an average diameter of almost 220 nm. Furthermore, the SEM-assisted element mapping image proved the presence of evenly distributed Cu, O, N, and C elements, which indicated the successful preparation of PDA@Cu NPs (Fig. 1E). Next, the UV–vis–NIR absorption spectra of prepared nanomaterials were checked. As can be seen from Fig. 1F, PDA@Cu NPs had a significantly higher absorption at 808 nm, revealing that PDA@Cu NPs may be more suitable for PTT. As expected, the PCE (η) of PDA and PDA@Cu NPs at 808 nm NIR, determined by equations (3)–(5), was 30.8% and 54.2% (Fig. 1G–H). This data suggested that the photothermal behavior of PDA NPs was remarkably enhanced after Cu deposition.

Next, the photothermal performance of PDA@Cu NPs under different powers (0.5, 1.0, and 2.0 W/cm^2) was studied. We observed from Fig. 1I that under the irradiation of the NIR laser (808 nm, 0.5 W/cm^2), the temperature (Δt) of PDA@Cu NPs increased from 0 °C to 10.5 °C within 3 min, and it achieved 18.1 °C within 6 min. With the increase of laser power, the temperature of PDA@Cu NPs enhanced to 40.2 °C (1.0 W/cm^2) and 61.9 °C (2.0 W/cm^2) after 6 min of irradiation. In addition, the PDA@Cu NPs maintained robust photothermal stability after multiple irradiation cycles because the maximum heating temperature was not significantly reduced (Fig. 1J). Similarly, the photothermal heating effect was observed from the infrared thermal images of PDA@Cu NPs (Fig. 1K). These results showed that the as-prepared PDA@Cu NPs possessed excellent photothermal performance that may have the potential as a photothermal antibacterial system for treating bacterial infections.

3.2. Synthesis and characterization of CPAP/PDA@Cu hydrogels

Polyelectrolyte hydrogel is a classical cross-linking system that enables fast cross-linking by multiple interactions (such as electrostatic force, hydrogen bonding, and hydrophobic interactions) between positively and negatively charged polymers without the use of additional cross-linking agents [38]. Herein, a polyelectrolyte hydrogel matrix composed of cationic polyethyleneimine/anionic pectin (labeled as CPAP) was employed to avoid the photothermal ability loss of PDA@Cu NPs caused by aggregation. Before confirming the use of polyethyleneimine and pectin, we tried different positively charged polymers (such as chitosan, polylysine, and polyethyleneimine) and negatively

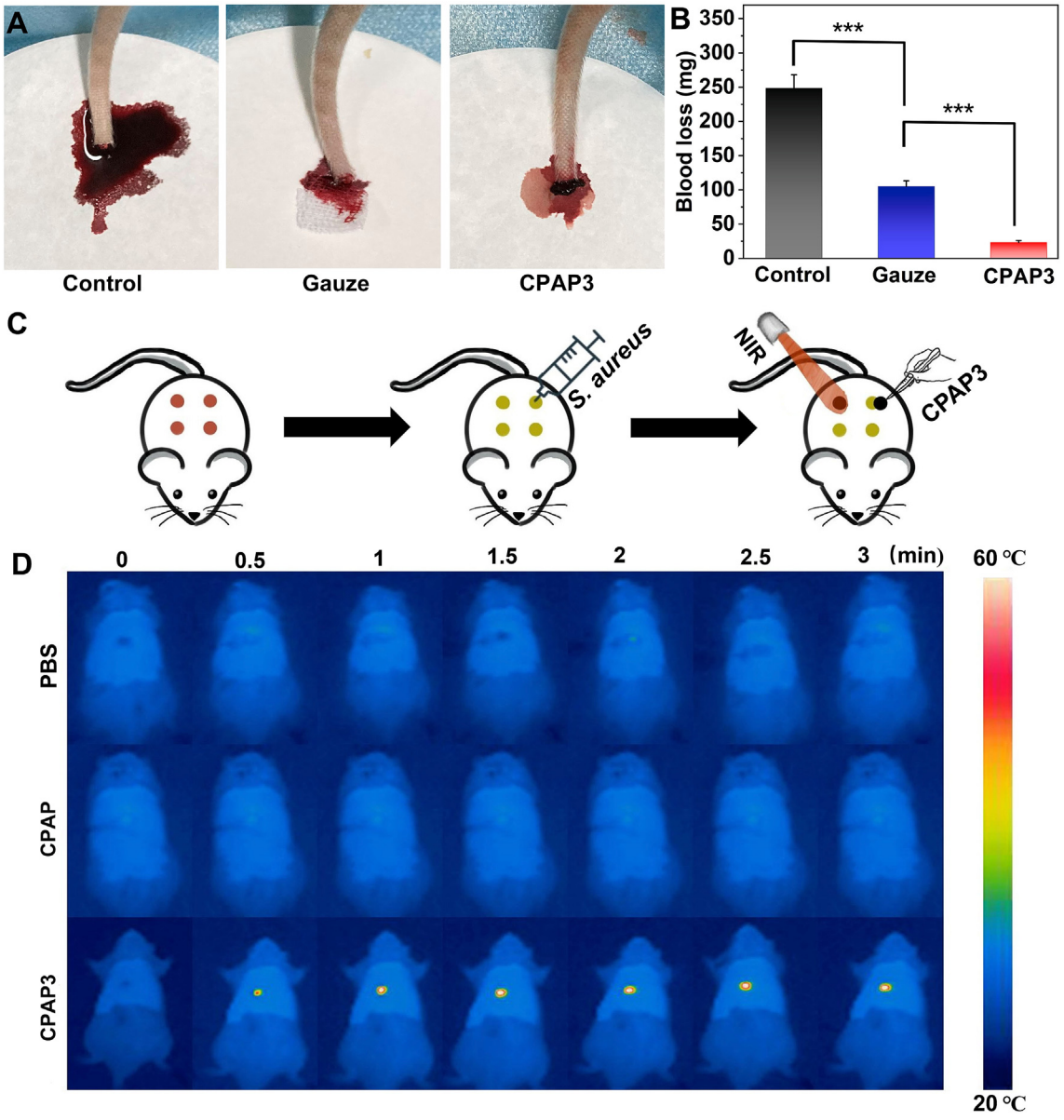

Fig. 6. *In vivo* assessment of hemostasis and photothermal performance of CPAP/PDA@Cu hydrogel. (A) Photographs displaying the materials after application to the rat-tail amputation model. (B) The hemostatic ability of the tested materials was determined by measuring the total blood loss in a rat-tail amputation model (n = 3, and ***P < 0.001). (C) Schematic of the *in vivo* wound treatment assay. (D) Infrared thermal images of rats at different time intervals.

charged polymers (such as hyaluronic acid, alginate, and pectin). However, except for polyethyleneimine/pectin, other systems required more demanding reaction conditions (such as an acidic environment and additional multivalent ions). Therefore, in the present work, we used polyethyleneimine/pectin to load PDA@Cu NPs. Three kinds of CPAP/PDA@Cu hydrogels (CPAP1, CPAP2, and CPAP3) were fabricated using an environmentally friendly one-pot blending approach. Typically, PDA@Cu NPs were first added to the anionic pectin (AP) solution, followed by the introduction of a cationic polyethyleneimine (CP) solution. The presence of multiple non-covalent interactions in the mixture (electrostatic force, π-π stacking, and hydrogen bonds) enabled the rapid transition of the precursor solution from sol to gel [39]. Of note, these recoverable non-covalent bonds can give the obtained hydrogel self-healing ability and injectability and provide more convenience for applying CPAP/PDA@Cu hydrogel in clinical practice.

We first determined the PCE (η) of PDA@Cu NPs and CPAP/PDA@Cu hydrogel at 808 nm. The η of PDA@Cu and CPAP/PDA@Cu (CPAP3) was 54.2% and 55.4% (Fig. S2) under the same concentration of PDA@Cu NPs. This confirmed our hypothesis that preventing aggregation and promoting dispersion of PDA@Cu NPs helped to enhance the photothermal properties of the resulting system. Therefore, CPAP3 with robust photothermal performance was chosen as the model specimen for the following antibacterial assay.

Subsequently, the functional groups of CPAP/PDA@Cu hydrogel were investigated by FTIR spectra. As shown in Fig. 2A, we observed that pure CPAP hydrogel and CPAP/PDA@Cu hydrogel had sugar ring, C–H, and O–H vibrations at approximately 1648, 2920, and 3200 cm^{-1}. More interestingly, the redshift in the CPAP hydrogel (from 3224 to 3190 cm^{-1}) after introducing PDA@Cu NPs may be due to the reason that the newly formed interactions (electrostatic interactions and π-π stacking) between PDA@Cu NPs and CPAP destroyed some of the previously established hydrogen bonds in the polyelectrolyte matrix, further proving the successful fusion of PDA@Cu NPs with the CPAP networks [40,41]. After that, a TGA assay was conducted to explore the thermal stability of CPAP specimens (Fig. 2B). The remaining mass of the CPAP3 at 600 °C was higher than that of the CPAP, confirming that the thermal

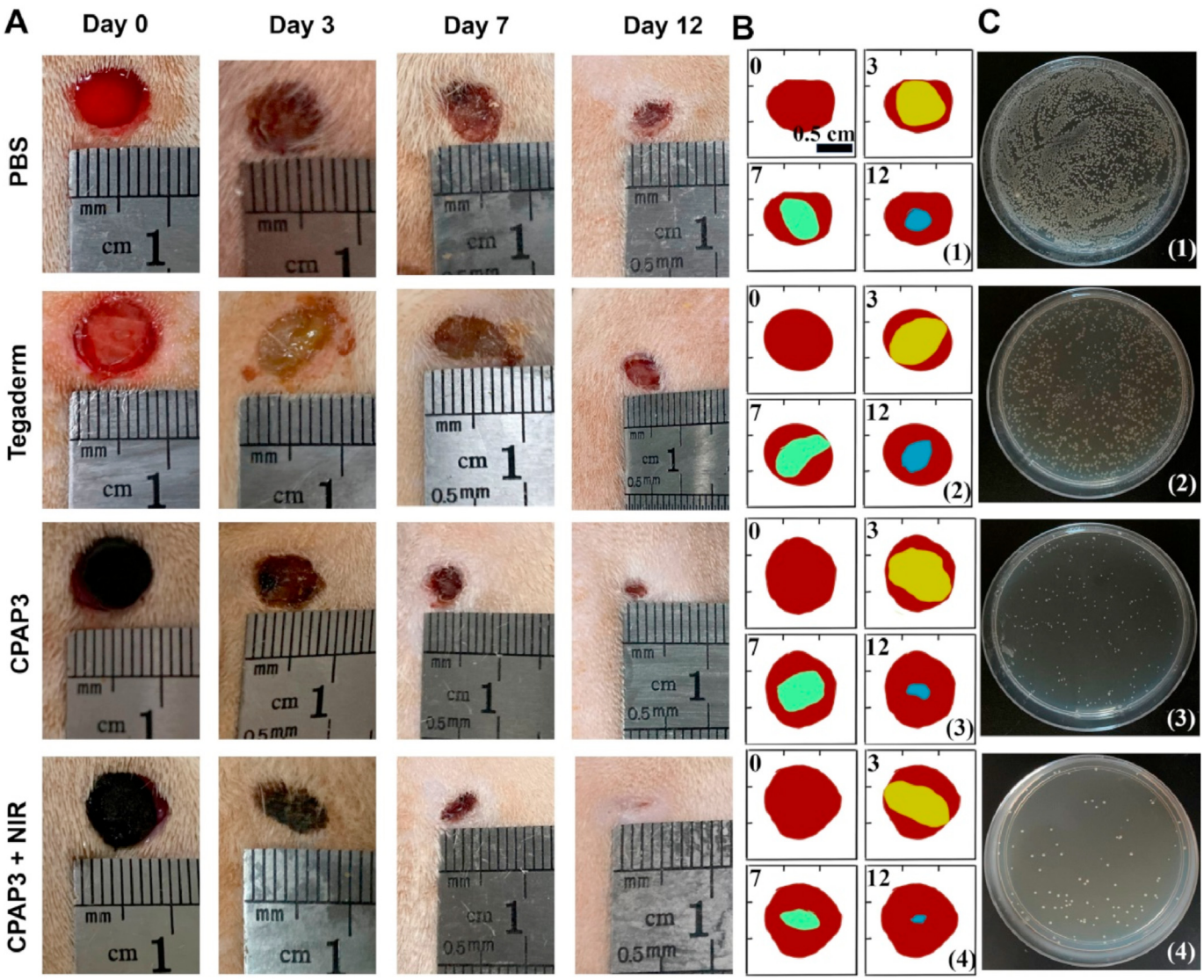

Fig. 7. *In vivo* evaluation of the wound healing properties. (A) Photographic images of different treatments of *S. aureus*-infected wounds from day 0–12. (B) Schematic representation of wound contraction treated with varying specimens from day 0–12: (1) PBS, (2) Tegaderm, (3) CPAP3, and (4) CPAP3 + NIR. (C) Images of bacterial colonies on agar plates from wound sites on the first day after different treatments: (1) PBS, (2) Tegaderm, (3) CPAP3, and (4) CPAP3 + NIR.

stability of the CPAP was improved due to the presence of PDA@Cu NPs. Then, the water uptake behavior of the hydrogel was investigated by culturing the prepared hydrogel in PBS until reaching the equilibrium state (Fig. 2C). The water absorption of CPAP and CPAP2 in the equilibrium state was 149.1 and 146.5, respectively, attributed to the increase in cross-linking density of the hydrogel. We speculated that after the PDA@Cu NPs were incorporated into the CPAP matrix, more non-covalent interactions involving electrostatic interactions formed in the hydrogel, resulting in a dense hydrogel network, which hindered the water uptake [42]. This meant that, compared with pure CPAP hydrogel, the water in CPAP2 was difficult to escape from the tight cross-linked hydrogel network, as demonstrated by the results of the water retention assay (Fig. 2D). Next, the architectural information of CPAP/PDA@Cu hydrogel was studied by SEM (Fig. 2E). After PDA@Cu NPs were loaded, the CPAP/PDA@Cu hydrogel presented a porous interconnected architecture, and a higher magnification SEM image confirmed that PDA@Cu NPs existed in the form of NPs inside the hydrogel. These data evidenced the successful fabrication of CPAP/PDA@Cu.

Typically, hydrogels used as wound dressings are required to possess a certain level of self-healing capability to cope with the pressure on the wounds caused by body movements, which will enhance the safety and use time of hydrogels [43,44]. Therefore, the mechanical and self-healing performance of the developed CPAP/PDA@Cu hydrogel was assessed. Briefly, rheological experiments were performed to evaluate the mechanical features of CPAP/PDA@Cu hydrogel. First, the hydrogel point of the prepared CPAP/PDA@Cu hydrogel was almost 20% (Fig. 3A). Then, the moduli of the CPAP/PDA@Cu hydrogel were studied. As presented in Fig. 3B, the dynamic frequency sweep assay results showed that the G′ was always larger than G″ when the angular frequency applied to hydrogel rose from 0.1 to 10 rad/s [45,46]. Besides, both G′ and G″ were not related to angular frequency, suggesting that elastic behavior of the CPAP/PDA@Cu hydrogel dominated the viscous one. Subsequently, the rheological recovery test was performed by determining G′ and G″ under different strains. The low strain was fixed at 1%, and the high strain was selected as 1000% (exceeding the critical points about fifty times). As displayed in Fig. 3C, when a high strain (1000%) was applied, G′ was lower than G″, demonstrating that the collapse of the CPAP/PDA@Cu hydrogel network occurred. On the other hand, when the used strain was 1%, G′ value increased sharply and immediately became bigger than G″, meaning the specimen returned to a gel state [47]. Meanwhile, G′ and G″ can restore to their initial values wholly without decrease after three repeated intervals, proving the remarkable self-healing capacity of

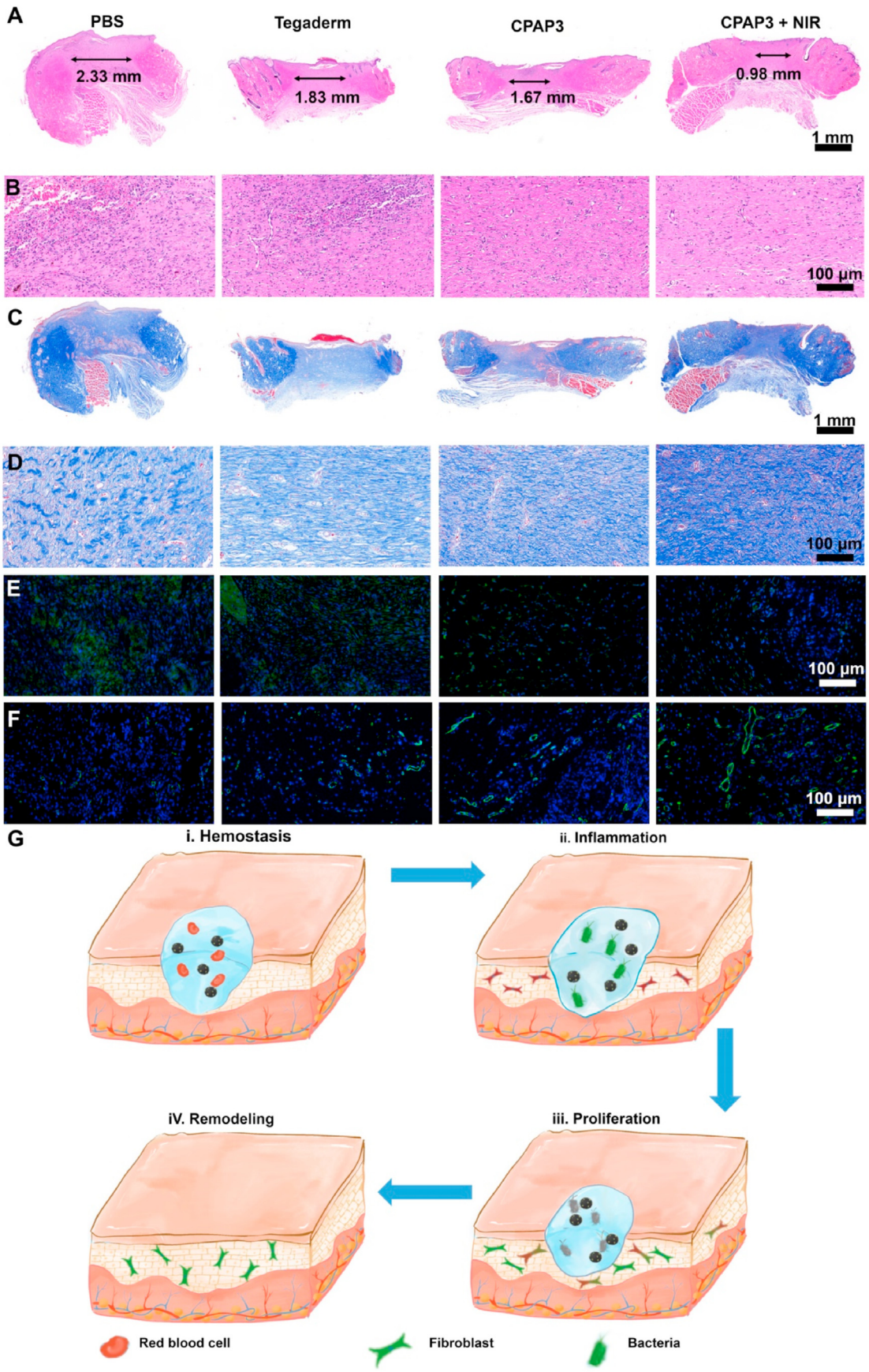

Fig. 8. Histological changes in newly regenerated skin after treating with different samples. Representative images of skin tissue slices after fluorescence labeling with H&E (A and B), Masson's trichrome (C and D), IL-6 (E), and CD31 (F). (G) Diagram of the potential wound healing mechanism of the prepared CPAP/PDA@Cu.

CPAP/PDA@Cu [48].

In addition, the self-healing capability of the CPAP/PDA@Cu was investigated. The CPAP/PDA@Cu hydrogel with column shape was first physically cut into two halves. Then, as shown in Fig. 3D, two hydrogel halves could recombine into a new hydrogel without noticeable break lines after being left for 2 h in environmental conditions without any external intervention. In addition, no significant difference between the original CPAP/PDA@Cu hydrogel and the healed CPAP/PDA@Cu hydrogel was observed. The excellent self-healing performance of CPAP/PDA@Cu hydrogel was due to the non-covalent interactions (electrostatic force, π-π stacking, and hydrogen bond) induced by the functional groups of CPAP and PDA@Cu NPs that can dynamically associate and disassociate (Fig. 3E).

3.3. Photothermal antibacterial activity of CPAP/PDA@Cu in vitro

First, the photothermal performance of CPAP/PDA@Cu (CPAP3) hydrogel was studied. We observed from Fig. S3 and S4 that under the 808 nm NIR irradiation (1.0 W/cm^2), CPAP/PDA@Cu hydrogel temperature (Δt) increased from 0 °C to 40.1 °C within 3 min, and it achieved 45.7 °C within 5 min. These results showed that the as-prepared CPAP/PDA@Cu hydrogel possessed excellent photothermal performance that may have the potential as a photothermal antibacterial system for treating bacterial infections.

The excellent light-to-heat conversion properties of the fabricated CPAP/PDA@Cu hydrogel motivated us to assess its antibacterial activity. In this study, we selected two strains of bacteria (*E. coli* and *S. aureus*) that were the culprit of most infectious diseases to investigate the antibacterial ability of CPAP/PDA@Cu. As shown in Fig. 4A, after contacting the hydrogel at 37 °C for 2 h, the CPAP hydrogel and CPAP/PDA@Cu hydrogel showed 80.2% and 34.6% survival rates for *S. aureus* (Fig. S5) and 71.1% and 22.4% survival rate for *E. coli* (Fig. S6), respectively. Therefore, we speculated that CPAP/PDA@Cu hydrogel possessing large positive groups (–NH_2) could interact with negatively bacterial cell membranes, leading to pathogen capture and inactivation. Besides, the antibacterial performance of CPAP/PDA@Cu hydrogel was better than that of CPAP hydrogel, which was ascribed to the antibacterial effect provided by PDA@Cu NPs. As anticipated, with the help of 808 nm NIR laser (1.0 W/cm^2, 5 min), most of *S. aureus* (>98.2%) and almost all *E. coli* (100%) were killed by the CPAP/PDA@Cu hydrogel. In addition, compared with the CPAP group, there was no significant improvement in antimicrobial performance after the introduction of NIR, which was due to the lack of photothermal warming sterilization properties of CPAP. These data exhibited that under the synergy of PDA@Cu NPs (photothermal sterilization) and CPAP hydrogel matrix (bacterial capture), the developed CPAP/PDA@Cu hydrogel possessed powerful antibacterial properties.

Subsequently, we conducted live/dead bacterial staining tests to identify potential antibacterial mechanisms of the CPAP/PDA@Cu (CPAP3) hydrogel. We found that fluorescence detection and plate count tests displayed the same antimicrobial trend. As exhibited in Fig. 4B and S7, both *S. aureus* and *E. coli* treated with PBS showed evident green fluorescence, and only a minority of bacteria were marked as red fluorescent. In comparison, some red fluorescence was observed in the CPAP, CPAP + NIR, and CPAP3; meanwhile, the CPAP3 + NIR group presented the most robust red fluorescence, revealing the optimum antibacterial effect.

Next, SEM was used to characterize the sterilization effect to explore the morphological changes of *S. aureus* and *E. coli* treated with different samples (Fig. 4C). Both *S. aureus* and *E. coli* with PBS treatment showed smooth and intact cell membranes, indicating negligible damage to bacteria from PBS [49]. In contrast, the bacteria were damaged to varying degrees after the hydrogel and hydrogel + NIR treatments. More specifically, some wrinkles presented in the CPAP/PDA@Cu hydrogel group, manifesting that the CPAP/PDA@Cu hydrogel had a specific antibacterial activity. This may be because the formulated polyelectrolyte hydrogel possessed some inherent antimicrobial properties that facilitated the antimicrobial effect by capturing and killing bacteria through effective interactions (such as electrostatic adsorption) between the CPAP/PDA@Cu and bacteria. However, there were still some well-shaped bacteria in the CPAP/PDA@Cu, demonstrating that the antibacterial capability of CPAP/PDA@Cu hydrogel was not enough to kill all bacteria (Fig. S8). More importantly, when CPAP/PDA@Cu was used with the assistance of an 808 nm NIR, the bacteria showed more severe damage, with deformed or even ruptured bacterial cell membrane, suggesting that the developed antibacterial system (CPAP/PDA@Cu + NIR) had the most significant bactericidal effect.

3.4. Cytotoxicity and hemolysis experiments

Biocompatibility is essential for *in vivo* antimicrobial applications of hydrogels [50]. First, the biocompatibility of the CPAP/PDA@Cu hydrogel was evaluated using a hemocompatibility assay. The supernatant of red blood cells treated with deionized water (DDW) was bright red, whereas those treated with PBS and CPAP/PDA@Cu hydrogel groups were colorless (Fig. 5A). Therefore, as displayed in Fig. 5B, the optical density (OD) of the hydrogel and PBS was much lower than that of the DDW group, demonstrating the negligible hemolytic effect of CPAP/PDA@Cu hydrogel [51]. Next, the cytotoxicity of CPAP/PDA@Cu hydrogels on L929 cells was evaluated by employing the CCK-8 assay. As presented in Fig. 5C and S9, similar to the control group, NIR treatment and CPAP/PDA@Cu hydrogels did not cause significant toxicity to L929 cells. Besides, we employed a live/dead cell staining technique to explore the cytocompatibility of the produced CPAP/PDA@Cu hydrogels. No significant red fluorescence was detected when culturing L929 cells with CPAP/PDA@Cu, indicating the non-toxic nature of CPAP/PDA@Cu hydrogels (Fig. 5D) [52]. Moreover, we also found that the designed CPAP/PDA@Cu (CPAP3) hydrogel possessed prominent hemostatic ability (Fig. 6A–B). For example, after 3 min of sample treatment, the blood weights of the PBS, gauze, and CPAP3 were 249.5 mg, 100.9 mg, and 24.7 mg, respectively. In sum, the CPAP/PDA@Cu hydrogel had excellent biocompatibility that may be suitable for *in vivo* anti-infection treatment.

3.5. In vivo antibacterial experiment

In this work, we used a rat bacteria-infected model to assess the *in vivo* antibacterial capability of the designed CPAP/PDA@Cu dressing (Fig. 6C). First, the *in vivo* photothermal performance of CPAP/PDA@Cu hydrogel was studied (Fig. 6D). After 808 nm NIR irradiation (1.0 W/cm^2) for 3 min, the wound area temperature (Δt) of the rat covered with CPAP/PDA@Cu hydrogel rose to 23.4 °C, while the local temperature of the PBS was only increased to 1.9 °C; besides, an agar plate colony counting method was used to detect bacteria at the wound site on the first day to estimate the sterilization performance of different samples (Fig. 7C and S10). As displayed in Fig. 7C, numerous bacteria appeared on the agar plates of the CPAP hydrogel and control groups. In contrast, almost no bacteria could be observed on the agar plates treated with CPAP/PDA@Cu + NIR, consistent with the *in vitro* antibacterial data, providing intuitive evidence that CPAP/PDA@Cu can be employed as a robust platform for *in vivo* antibacterial treatment.

Subsequently, the wound healing process of *S. aureus*-infected wounds managed with different specimens (PBS, Tegaderm hydrogel, CPAP/PDA@Cu hydrogel, and CPAP/PDA@Cu hydrogel + NIR) was photographed by a digital camera (Fig. 7A). The schematic diagram of wound contraction is shown in Fig. 7B. The wound size gradually decreased over time for all test groups. On day 12, the open wounds in the CPAP/PDA@Cu + NIR group were the smallest (3.4%) and possessed some newly regenerated epidermis, while 10.2%, 32.1%, and 38.4% of the wounds remained unhealed with prominent scars in the CPAP/PDA@Cu hydrogel, Tegaderm hydrogel and PBS groups (Fig. S11). These results showed that the CPAP/PDA@Cu + NIR group had the greatest

healing effect compared to other groups. Under the synergistic effect of the photothermal properties of PDA@Cu NPs and the inherent antibacterial activity of CPAP hydrogels, CPAP/PDA@Cu hydrogel exhibited optimal antibacterial properties, which effectively killed pathogens and accelerated the wound healing process (Fig. S12). Besides, some additional functions offered by the CPAP/PDA@Cu hydrogel at the wound site, such as hemostasis (Fig. 6A), gas exchange, adsorption of exudate, acting as a physical barrier, and serving as a cell scaffold, also had benefits for improving skin regeneration [45,53].

Finally, the histological changes in skin tissues during the wound healing process were investigated to better understand the internal mechanism of wound repair. Skin tissues were collected at a pre-set time after different treatments (PBS, Tegaderm hydrogel, CPAP/PDA@Cu hydrogel, and CPAP/PDA@Cu hydrogel + NIR) and stained by H&E (Fig. 8A and B), Masson (Fig. 8C and D), IL-6 (Fig. 8E), and CD31 (Fig. 8F). The results of H&E revealed that on day 12, the wound scar width in CPAP/PDA@Cu + NIR (0.98 mm) was the smallest compared with the PBS (2.33 mm), Tegaderm (1.83 mm), and CPAP3 (1.67 mm) groups; from the high magnification H&E photos, we found that wounds treated with CPAP3 and control groups showed many inflammatory signals (neutrophils and blood cells), while wounds in the CPAP/PDA@Cu + NIR group had no significant inflammation and possessed regenerated dermal tissues and hair follicles (Fig. 8A and B). Besides, compared with other groups, more collagen fibers were observed in the CPAP/PDA@Cu + NIR group (Fig. 8C and D). Additionally, the expression of IL-6 inflammatory markers in wounds of the CPAP/PDA@Cu + NIR group was significantly lower than that of the other three groups (Fig. S13). Moreover, the NIR-assisted CPAP/PDA@Cu system displayed the highest expression of CD31 compared to the other three tested groups, indicating that the CPAP/PDA@Cu + NIR group had the best pro-angiogenic capability (Fig. S14). In conclusion, CPAP/PDA@Cu + NIR promoted the transition from the hemostatic phase to the inflammatory, proliferative, and remodeling phases of the wound, resulting in regenerated skin with low inflammation, high collagen fibers, thick granulation, and newborn hair follicles (Fig. 8G). These data indicate that the NIR-assisted CPAP/PDA@Cu system is a hopeful platform for photothermal therapy of bacterial infections.

4. Conclusion

Summarized, for the first time, we successfully developed a high-performance antibacterial platform (CPAP/PDA@Cu). PDA@Cu nanoPTAs were first constructed by growing Cu NPs in situ on the surface of PDA NPs using a facile one-pot reduction deposition method, and then they were evenly dispersed in the CPAP hydrogel matrix by an easy mixing approach. Thanks to the inherent bacterial capture/killing capability of the CPAP hydrogel and the robust photothermal performance ($\eta = 55.4\%$) of CPAP/PDA@Cu, a highly efficient, convenient, broad-spectrum, and environmentally friendly antibacterial system was fabricated, not only achieving bactericidal activity against *S. aureus* (98.2%) and *E. coli* (100%) *in vitro* but also ensuring outstanding high-efficiency bacteria-killing capability *in vivo*. This study opens a new avenue for PTT to design high-performance PDA photothermal nanomaterials.

Author statement

ZhangPing Li: Investigation, Methodology. **Shengye You**: Investigation, Formal analysis. **Ruiting Mao**: Formal analysis. **Yajing Xiang**: Methodology. **Erya Cai**: Investigation. **Hui Deng**: Investigation. **Jianliang Shen**: Supervision. **Xiaoliang Qi**: Conceptualization, Writing – original draft.

Declaration of competing interest

The authors declare that they have no known competing financial interests or personal relationships that could have appeared to influence the work reported in this paper.

Acknowledgments

This work was partially supported by the Natural Science Foundation of Zhejiang Province (LQ22E030011) and Wenzhou Medical University (KYYW201901and KYYW201906).

Appendix A. Supplementary data

Supplementary data to this article can be found online at https://XXX.

Appendix B. Supplementary data

Supplementary data to this article can be found online at https://doi.org/10.1016/j.mtbio.2022.100264.

References

[1] L.X. Yan, L.J. Chen, X. Zhao, X.P. Yan, pH switchable nanoplatform for in vivo persistent luminescence imaging and precise photothermal therapy of bacterial infection, Adv. Funct. Mater. 30 (2020) 1909042, https://doi.org/10.1002/adfm.201909042.

[2] J. Niu, Y. Sun, F. Wang, C. Zhao, J. Ren, X. Qu, Photomodulated nanozyme used for a gram-selective antimicrobial, Chem. Mater. 30 (2018) 7027–7033, https://doi.org/10.1021/acs.chemmater.8b02365.

[3] R. Gannimani, P. Walvekar, V.R. Naidu, T.M. Aminabhavi, T. Govender, Acetal containing polymers as pH-responsive nano-drug delivery systems, J. Contr. Release 328 (2020) 736–761, https://doi.org/10.1016/j.jconrel.2020.09.044.

[4] D. Liu, X. Ma, Y. Ji, R. Chen, S. Zhou, H. Yao, Z. Zhang, M. Ye, Z. Xu, M. Du, Bioresponsive nanotherapy for preventing dental caries by inhibiting multispecies cariogenic biofilms, Bioact. Mater. 14 (2022) 1–14, https://doi.org/10.1016/j.bioactmat.2021.12.016.

[5] J. Li, Y. Wang, J. Yang, W. Liu, Bacteria activated-macrophage membrane-coated tough nanocomposite hydrogel with targeted photothermal antibacterial ability for infected wound healing, Chem. Eng. J. 420 (2021) 127638, https://doi.org/10.1016/j.cej.2020.127638.

[6] X. Shi, X. Ma, E. Ren, Y. Zhang, D. Jia, Y. Gao, P. Xue, Y. Kang, G. Liu, Z. Xu, Tumor-Microenvironment-Activatable nanoreactor based on a polyprodrug for multimodal-imaging-medicated enhanced cancer chemo/phototherapy, ACS Appl. Mater. Interfaces 11 (2019) 40704–40715, https://doi.org/10.1021/acsami.9b16054.

[7] F. Zhang, G. Lu, X. Wen, F. Li, X. Ji, Q. Li, M. Wu, Q. Cheng, Y. Yu, J. Tang, L. Mei, Magnetic nanoparticles coated with polyphenols for spatio-temporally controlled cancer photothermal/immunotherapy, J. Contr. Release 326 (2020) 131–139, https://doi.org/10.1016/j.jconrel.2020.06.015.

[8] Z. Li, Y. Yang, H. Wei, X. Shan, X. Wang, M. Ou, Q. Liu, N. Gao, H. Chen, L. Mei, X. Zeng, Charge-reversal biodegradable MSNs for tumor synergetic chemo/photothermal and visualized therapy, J. Contr. Release 338 (2021) 719–730, https://doi.org/10.1016/j.jconrel.2021.09.005.

[9] J. Su, S. Lu, S. Jiang, B. Li, B. Liu, Q. Sun, J. Li, F. Wang, Y. Wei, Engineered protein photo-thermal hydrogels for outstanding in situ tongue cancer therapy, Adv. Mater. 33 (2021) 2100619, https://doi.org/10.1002/adma.202100619.

[10] Q. Fang, K. Xu, Q. Xiong, Y. Xu, A. Hui, S. Xuan, Fe_3O_4–Au–polydopamine hybrid microcapsules with photothermal–photodynamic synergistic anti-bacterial performance, CrystEngComm 23 (2021) 6610–6619, https://doi.org/10.1039/d1ce00926e.

[11] N. Yang, H. Guo, C. Cao, X. Wang, X. Song, W. Wang, D. Yang, L. Xi, X. Mou, X. Dong, Infection microenvironment-activated nanoparticles for NIR-II photoacoustic imaging-guided photothermal/chemodynamic synergistic anti-infective therapy, Biomaterials 275 (2021) 120918, https://doi.org/10.1016/j.biomaterials.2021.120918.

[12] X. Zeng, M. Luo, G. Liu, X. Wang, W. Tao, Y. Lin, X. Ji, L. Nie, L. Mei, Polydopamine-modified black phosphorous nanocapsule with enhanced stability and photothermal performance for tumor multimodal treatments, Adv. Sci. 5 (2018) 1800510, https://doi.org/10.1002/advs.201800510.

[13] L. Jin, H. Cheng, X. Xie, X. Chen, G. Tian, Z. Zhu, S. Wang, H. Xin, X. Wang, Dual-effective chronic wounds management system through a monoglyceride binary blend matrix based thermal-responsive phase-transition substrate, Adv. Healthc. Mater. 10 (2021) 2001966, https://doi.org/10.1002/adhm.202001966.

[14] S.M. Yu, G.W. Li, R. Liu, D. Ma, W. Xue, Dendritic Fe_3O_4@Poly(dopamine)@PAMAM nanocomposite as controllable NO-releasing material: a synergistic

photothermal and NO antibacterial study, Adv. Funct. Mater. 28 (2018) 1707440, https://doi.org/10.1002/adfm.201707440.
[15] Y. Fu, L. Yang, J. Zhang, J. Hu, G. Duan, X. Liu, Y. Li, Z. Gu, Polydopamine antibacterial materials, Mater. Horiz. 8 (2021) 1618–1633, https://doi.org/10.1039/d0mh01985b.
[16] H. Miao, R. Shen, W. Zhang, Z. Lin, H. Wang, L. Yang, X.Y. Liu, N. Lin, Near-infrared light triggered silk fibroin scaffold for photothermal therapy and tissue repair of bone tumors, Adv. Funct. Mater. 31 (2021) 2007188, https://doi.org/10.1002/adfm.202007188.
[17] Y. Liu, Q. Fan, Y. Huo, C. Liu, B. Li, Y. Li, Construction of a mesoporous polydopamine@GO/cellulose nanofibril composite hydrogel with an encapsulation structure for controllable drug release and toxicity shielding, ACS Appl. Mater. Interfaces 12 (2020) 57410–57420, https://doi.org/10.1021/acsami.0c15465.
[18] P. Yang, F. Zhu, Z. Zhang, Y. Cheng, Z. Wang, Y. Li, Stimuli-responsive polydopamine-based smart materials, Chem. Soc. Rev. 50 (2021) 8319–8343, https://doi.org/10.1039/d1cs00374g.
[19] H. Gholami Derami, P. Gupta, K.C. Weng, A. Seth, R. Gupta, J.R. Silva, B. Raman, S. Singamaneni, Reversible photothermal modulation of electrical activity of excitable cells using polydopamine nanoparticles, Adv. Mater. 33 (2021) 2008809, https://doi.org/10.1002/adma.202008809.
[20] F. Liu, X. He, J. Zhang, H. Chen, H. Zhang, Z. Wang, Controllable synthesis of polydopamine nanoparticles in microemulsions with pH-activatable properties for cancer detection and treatment, J. Mater. Chem. B 3 (2015) 6731–6739, https://doi.org/10.1039/c5tb01159k.
[21] L.P. Ferreira, V.M. Gaspar, M.V. Monteiro, B. Freitas, N.J.O. Silva, J.F. Mano, Screening of dual chemo-photothermal cellular nanotherapies in organotypic breast cancer 3D spheroids, J. Contr. Release 331 (2021) 85–102, https://doi.org/10.1016/j.jconrel.2020.12.054.
[22] D. Xi, M. Xiao, J. Cao, L. Zhao, N. Xu, S. Long, J. Fan, K. Shao, W. Sun, X. Yan, X. Peng, NIR light-driving barrier-free group rotation in nanoparticles with an 88.3% photothermal conversion efficiency for photothermal therapy, Adv. Mater. 32 (2020) 1907855, https://doi.org/10.1002/adma.201907855.
[23] Y. Zou, X. Chen, P. Yang, G. Liang, Y. Yang, Z. Gu, Y. Li, Regulating the absorption spectrum of polydopamine, Sci. Adv. 6 (2020), eabb4696, https://doi.org/10.1126/sciadv.abb4696.
[24] Z. Wang, Y. Zou, Y. Li, Y. Cheng, Metal-containing polydopamine nanomaterials: catalysis, energy, and theranostics, Small 16 (2020) 1907042, https://doi.org/10.1002/smll.201907042.
[25] X. Qi, W. Pan, X. Tong, T. Gao, Y. Xiang, S. You, R. Mao, J. Chi, R. Hu, W. Zhang, H. Deng, J. Shen, ε-Polylysine-stabilized agarose/polydopamine hydrogel dressings with robust photothermal property for wound healing, Carbohydr. Polym. 264 (2021) 118046, https://doi.org/10.1016/j.carbpol.2021.118046.
[26] D. Cheng, X. Bai, J. Pan, J. Wu, J. Ran, G. Cai, X. Wang, In situ hydrothermal growth of Cu NPs on knitted fabrics through polydopamine templates for heating and sensing, Chem. Eng. J. 382 (2020) 123036, https://doi.org/10.1016/j.cej.2019.123036.
[27] Y. Zou, T. Wu, N. Li, X. Guo, Y. Li, Photothermal-enhanced synthetic melanin inks for near-infrared imaging, Polymer 186 (2020), https://doi.org/10.1016/j.polymer.2019.122042.
[28] W. Cheng, X. Zeng, H. Chen, Z. Li, W. Zeng, L. Mei, Y. Zhao, Versatile polydopamine platforms: synthesis and promising applications for surface modification and advanced nanomedicine, ACS Nano 13 (2019) 8537–8565, https://doi.org/10.1021/acsnano.9b04436.
[29] T. Salvador, M.B. Oliveira, J.F. Mano, Leachable-free fabrication of hydrogel foams enabling homogeneous viability of encapsulated cells in large-volume constructs, Adv. Healthc. Mater. 9 (2020) 2000543, https://doi.org/10.1002/adhm.202000543.
[30] B. Tian, S. Liu, L. Feng, S. Liu, S. Gai, Y. Dai, L. Xie, B. Liu, P. Yang, Y. Zhao, Renal-clearable nickel-doped carbon dots with boosted photothermal conversion efficiency for multimodal imaging-guided cancer therapy in the second near-infrared biowindow, Adv. Funct. Mater. 31 (2021) 2100549, https://doi.org/10.1002/adfm.202100549.
[31] G. Liu, Q. Xiong, Y. Xu, Q. Fang, K.C.-F. Leung, M. Sang, S. Xuan, L. Hao, Sandwich-structured MXene@Au/polydopamine nanosheets with excellent photothermal-enhancing catalytic activity, Colloid. Surface. 633 (2022) 127860, https://doi.org/10.1016/j.colsurfa.2021.127860.
[32] K. Feng, L. Peng, L. Yu, Y. Zheng, R. Chen, W. Zhang, G. Chen, Universal antifogging and antimicrobial thin coating based on dopamine-containing glycopolymers, ACS Appl. Mater. Interfaces 12 (2020) 27632–27639, https://doi.org/10.1021/acsami.0c07949.
[33] Y. Li, T. Gong, H. Gao, Y. Chen, H. Li, P. Zhao, Y. Jiang, K. Wang, Y. Wu, X. Zheng, W. Bu, ZIF-Based nanoparticles combine X-ray-induced nitrosative stress with autophagy management for hypoxic prostate cancer therapy, Angew. Chem. Int. Ed. 60 (2021) 15472–15481, https://doi.org/10.1002/anie.202103015.
[34] Q. Ou, S. Zhang, C. Fu, L. Yu, P. Xin, Z. Gu, Z. Cao, J. Wu, Y. Wang, More natural more better: triple natural anti-oxidant puerarin/ferulic acid/polydopamine incorporated hydrogel for wound healing, J. Nanobiotechnol. 19 (2021) 237, https://doi.org/10.1186/s12951-021-00973-7.
[35] M. Liang, Y. Gao, W. Qiu, M. Ye, J. Hu, J. Xu, P. Xue, Y. Kang, Z. Xu, Acid-sensitive supramolecular nanoassemblies with multivalent interaction: effective tumor retention and deep intratumor infiltration, ACS Appl. Mater. Interfaces 13 (2021) 37680–37692, https://doi.org/10.1021/acsami.1c10064.
[36] Q. Yuan, J. Huang, C. Xian, J. Wu, Amino acid- and growth factor-based multifunctional nanocapsules for the modulation of the local microenvironment in tissue engineering, ACS Appl. Mater. Interfaces 13 (2021) 2165–2178, https://doi.org/10.1021/acsami.0c15133.
[37] M.T. Tavares, S.C. Santos, C.A. Custodio, J.P.S. Farinha, C. Baleizao, J.F. Mano, Platelet lysates-based hydrogels incorporating bioactive mesoporous silica nanoparticles for stem cell osteogenic differentiation, Mater. Today Bio 9 (2021) 100096, https://doi.org/10.1016/j.mtbio.2021.100096.
[38] W. Xue, B. Liu, H. Zhang, S. Ryu, M. Kuss, D. Shukla, G. Hu, W. Shi, X. Jiang, Y. Lei, B. Duan, Controllable fabrication of alginate/poly-L-ornithine polyelectrolyte complex hydrogel networks as therapeutic drug and cell carriers, Acta Biomater. 138 (2022) 182–192, https://doi.org/10.1016/j.actbio.2021.11.004.
[39] U. Bozuyuk, N.O. Dogan, S. Kizilel, Deep insight into PEGylation of bioadhesive chitosan nanoparticles: sensitivity study for the key parameters through artificial neural network model, ACS Appl. Mater. Interfaces 10 (2018) 33945–33955, https://doi.org/10.1021/acsami.8b11178.
[40] X. Pan, S. Cheng, C. Zhang, Y. Jiao, X. Lin, W. Dong, X. Qi, Mussel-inspired magnetic pullulan hydrogels for enhancing catalytic degradation of antibiotics from biomedical wastewater, Chem. Eng. J. 409 (2021) 128203, https://doi.org/10.1016/j.cej.2020.128203.
[41] M. Wang, C. Wang, M. Chen, Y. Xi, W. Cheng, C. Mao, T. Xu, X. Zhang, C. Lin, W. Gao, Y. Guo, B. Lei, Efficient angiogenesis-based diabetic wound healing/skin reconstruction through bioactive antibacterial adhesive ultraviolet shielding nanodressing with exosome release, ACS Nano 13 (2019) 10279–10293, https://doi.org/10.1021/acsnano.9b03656.
[42] K.J. Ornell, D. Lozada, N.V. Phan, J.M. Coburn, Controlling methacryloyl substitution of chondroitin sulfate: injectable hydrogels with tunable long-term drug release profiles, J. Mater. Chem. B 7 (2019) 2151–2161, https://doi.org/10.1039/c8tb03020k.
[43] S. Wang, H. Zheng, L. Zhou, F. Cheng, Z. Liu, H. Zhang, L. Wang, Q. Zhang, Nanoenzyme-reinforced injectable hydrogel for healing diabetic wounds infected with multidrug resistant bacteria, Nano Lett. 20 (2020) 5149–5158, https://doi.org/10.1021/acs.nanolett.0c01371.
[44] Z. Yang, R. Huang, B. Zheng, W. Guo, C. Li, W. He, Y. Wei, Y. Du, H. Wang, D. Wu, H. Wang, Highly stretchable, adhesive, biocompatible, and antibacterial hydrogel dressings for wound healing, Adv. Sci. 8 (2021) 2003627, https://doi.org/10.1002/advs.202003627.
[45] M. Li, Y. Liang, J. He, H. Zhang, B. Guo, Two-pronged strategy of biomechanically active and biochemically multifunctional hydrogel wound dressing to accelerate wound closure and wound healing, Chem. Mater. 32 (2020) 9937–9953, https://doi.org/10.1021/acs.chemmater.0c02823.
[46] X. Ding, G. Li, P. Zhang, E. Jin, C. Xiao, X. Chen, Injectable self-healing hydrogel wound dressing with cysteine-specific on-demand dissolution property based on tandem dynamic covalent bonds, Adv. Funct. Mater. 31 (2021) 2011230, https://doi.org/10.1002/adfm.202011230.
[47] Z. Feng, Q. Su, C. Zhang, P. Huang, H. Song, A. Dong, D. Kong, W. Wang, Bioinspired nanofibrous glycopeptide hydrogel dressing for accelerating wound healing: a cytokine-free, M2-type macrophage polarization approach, Adv. Funct. Mater. 30 (2020) 2006454, https://doi.org/10.1002/adfm.202006454.
[48] M. Zheng, X. Wang, O. Yue, M. Hou, H. Zhang, S. Beyer, A.M. Blocki, Q. Wang, G. Gong, X. Liu, J. Guo, Skin-inspired gelatin-based flexible bio-electronic hydrogel for wound healing promotion and motion sensing, Biomaterials 276 (2021) 121026, https://doi.org/10.1016/j.biomaterials.2021.121026.
[49] Q. Xiong, Q. Fang, K. Xu, G. Liu, M. Sang, Y. Xu, L. Hao, S. Xuan, Near-infrared light-responsive photothermal α-Fe_2O_3@Au/PDA core/shell nanostructure with on-off controllable anti-bacterial effects, Dalton Trans. 50 (2021) 14235–14243, https://doi.org/10.1039/d1dt02251b.
[50] K. Lei, K. Wang, Y. Sun, Z. Zheng, X. Wang, Rapid-fabricated and recoverable dual-network hydrogel with inherently anti-bacterial abilities for potential adhesive dressings, Adv. Funct. Mater. 31 (2020) 2008010, https://doi.org/10.1002/adfm.202008010.
[51] W. Huang, S. Cheng, X. Wang, Y. Zhang, L. Chen, L. Zhang, Noncompressible hemostasis and bone regeneration induced by an absorbable bioadhesive self-healing hydrogel, Adv. Funct. Mater. 31 (2021) 2009189, https://doi.org/10.1002/adfm.202009189.
[52] W. Zeng, H. Zhang, Y. Deng, A. Jiang, X. Bao, M. Guo, Z. Li, M. Wu, X. Ji, X. Zeng, L. Mei, Dual-response oxygen-generating MnO_2 nanoparticles with polydopamine modification for combined photothermal-photodynamic therapy, Chem. Eng. J. 389 (2020) 124494, https://doi.org/10.1016/j.cej.2020.124494.
[53] L. Zhang, M. Liu, Y. Zhang, R. Pei, Recent progress of highly adhesive hydrogels as wound dressings, Biomacromolecules 21 (2020) 3966–3983, https://doi.org/10.1021/acs.biomac.0c01069.